Title

Understanding Molecular Structure and Diffusion Dynamics of Nanoconfined Water in Imogolite Nanotubes

Journal

Goldschmidt2025 abstracts

Authors

Fleming, Xander
Giovine, Raynald
Singh, Navya
et al.

Publication Date

2025

DOI

10.7185/gold2025.32252

Peer reviewed

JACS
JOURNAL OF THE AMERICAN CHEMICAL SOCIETY
pubs.acs.org/JACS

Article

Surface Hydroxyls of Imogolite Nanotubes Drive Distinct Structures and Mobility Differentiation of Nanoconfined Water

Xander B. Fleming, Sophia N. Fricke, Navya Singh, Raynald Giovine, Pierre Picot, Hasan Celik, Jeffrey A. Reimer, Benjamin Gilbert, and Zhao Hao*

Cite This: https://doi.org/10.1021/jacs.5c22784

ABSTRACT: Nanoconfined fluids, particularly water, govern subsurface geochemistry, yet the molecular-level mechanisms by which mineral surfaces dictate confined water structure and mobility remain poorly resolved. Here, we combine solution- and solid-state proton (^{1}H) NMR spectroscopy, NMR relaxometry, modulated-gradient spin−echo (MGSE) NMR diffusometry, infrared spectroscopy, and molecular dynamics simulations to demonstrate that surface hydroxyls drive the structural and dynamic differentiation of water in imogolite nanotubes. In saturated suspensions, we observe the coexistence of distinct water ^{1}H environments, each exhibiting significantly reduced mobility, which we attribute to strong interactions with the imogolite surfaces. As more mobile water is removed, long-range water diffusivity in the fibrous solid samples slows to 1.6×10^{-10} $m^2 \cdot s^{-1}$ while local fluctuations increase to 3.4×10^{-8} $m^2 \cdot s^{-1}$, indicating a significant increase in molecular restriction through surface interactions. Together, our experiments reveal three coexisting populations with varied structures and mobilities, all distinct from liquid bulk water. We resolve a persistent solid-like interfacial layer strongly bound to surface hydroxyls, characterized by an unusually short T_2 (<1 ms), and a very close effective ^{1}H−^{1}H distance of ∼1.55 Å between water and the inner-surface silanol group. An inner-core population occupying the inner cavity exhibits an intermediate dynamic regime with restricted axial diffusion, while outer-surface water associated with aluminum hydroxyls retains relatively higher mobility. These results experimentally substantiate a hierarchy of water populations in imogolite and show how surface chemistry dictates the structures and dynamics of confined water.

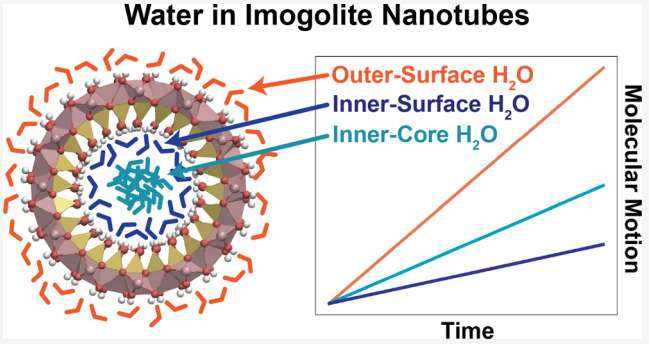

INTRODUCTION

Water is essential to life on Earth and governs fundamental processes in chemical, biological, and geological systems. When confined to nanoscale environments such as pores, channels, or interfacial layers, water exhibits dynamic and physical behaviors that differ from those of unrestricted bulk water.[1−3] These include altered phase transitions,[4−6] molecular mobility,[7−11] and dielectric properties.[12−15] Studies show that nanoconfined water exhibits a markedly reduced dielectric permittivity, which shifts ion solvation free energies,[16] alters mineral solubility, and governs fluid−rock interactions.[17] In nanometer-scale pore spaces, the structure of nanoconfined water controls guest molecule mobility, with substrate-specific solvation and hydrogen bonding dictating both selectivity and permeability.[18] Nanoconfinement modulates ion transport by restructuring the solvation environment, transport pathways, and stability of ions.[19] The presence of nanoconfined water influences many other subsurface geochemical processes, including the mineralization of carbon dioxide.[20,21]

A growing body of work has clarified that many of these effects are governed by the chemical properties of the interface, rather than geometric constraints from nanoconfinement. Computational studies show that the dielectric suppression of nanoconfined water is primarily an interfacial effect arising from surface-induced dipoles[14,22] and that the thermodynamics of water autoionization under nanoconfinement are tuned by the strength of water−wall interactions.[23] Recent experimental evidence demonstrates that for weakly confined water with nonbulk-like properties, the structure and hydrogen-bond network are governed primarily by interfacial effects, with significant nanoconfinement effects emerging at angstrom-scale (<∼8 Å) dimensions.[24] This distinction carries consequences for dissolved species in nanoscale geochemical systems—while ions in bulk solution always interact with an interfacial hydration layer, in nanoconfined environments, this interfacial

Received: December 23, 2025
Revised: July 15, 2026
Accepted: July 16, 2026

https://doi.org/10.1021/jacs.5c22784
J. Am. Chem. Soc. XXXX, XXX, XXX−XXX

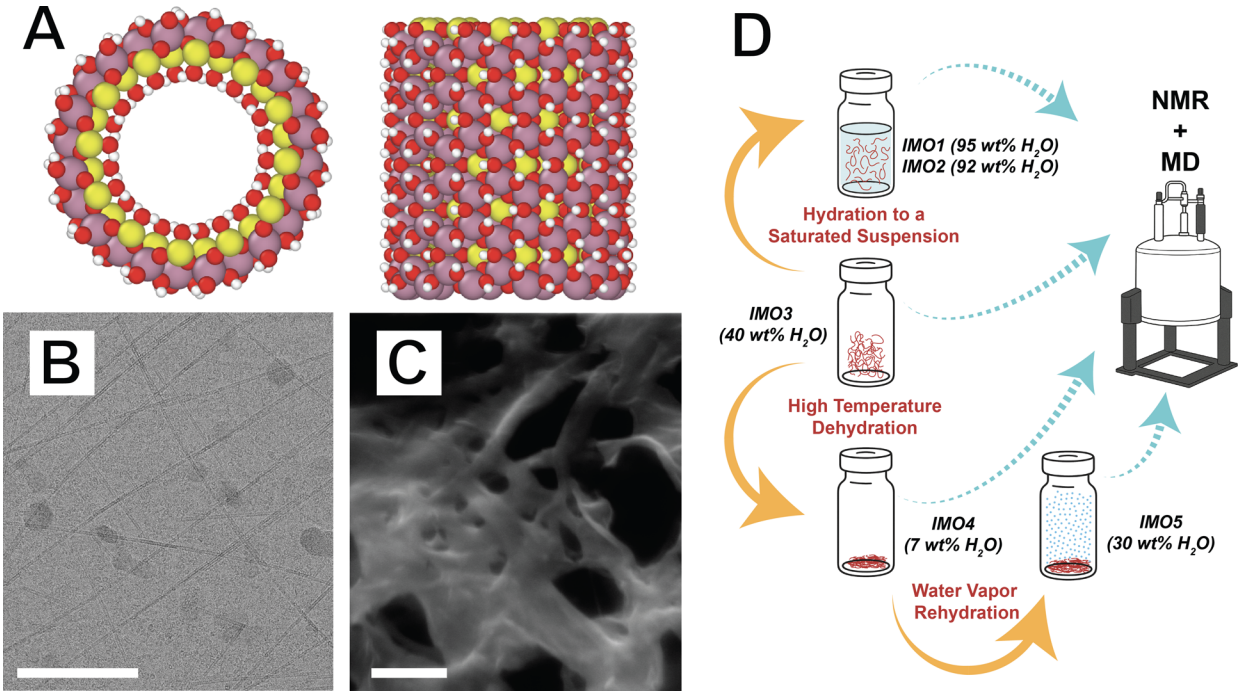

Figure 1. IMO nanotubes. (A) IMO structure composed of outer aluminum (pink), inner silicon (yellow), oxygen (red), and hydrogen (white). (B) Cryo-TEM image of synthetic IMO. The scale bar represents 100 nm. (C) SEM image of fibrous IMO clusters (light-colored areas, sample *IMO3*) deposited on a gold-coated substrate. The scale bar represents 10 μm. (D) Schematic illustration of IMO sample preparation and analysis.

layer becomes the dominant medium for transport and reactivity. Investigations of organic acids in silanol-rich nanopores have demonstrated measurable increases in pK_a under nanoconfinement, attributed to reduced dielectric response and proton accumulation within the pore volume even in the absence of direct acid-surface adsorption.[25]

Despite recent progress, a molecular-level understanding of how water−mineral interfaces influence the properties of nanoconfined fluids remains incomplete, mainly due to the complexity of natural systems. To address this, we employ imogolite (IMO) as a model system for studying nanoconfined water. IMO is a naturally occurring aluminosilicate nanotube, with the formula $(HO)_3Al_2O_3Si(OH)$, discovered in volcanic soils.[26,27] As shown in Figure 1A, IMO features an inner surface composed of isolated silicon tetrahedra and an outer surface formed of aluminum octahedra. IMO can extend several microns in length (Figure 1B) and can be synthesized with a larger diameter than natural analogues (internal and external diameters of ∼1.6 nm and ∼2.6 nm for our synthetic samples).[28] IMO surfaces are highly hydrophilic and densely hydroxylated, with 6.6 OH·nm^{-2} and 12.6 OH·nm^{-2} for internal and external surfaces, respectively.[28,29] When dried, the nanotubes tend to aggregate and form fibrous clusters (Figure 1C), creating a network of interstitial spaces with varying sizes and geometries.[30] This combination of uniform nanoscale confinement and chemically active interfaces makes IMOs ideally suited for probing the behavior of surface-bound and nanoconfined water.

Molecular dynamics (MD) simulations of IMO have shown that water confined within the nanotubes forms highly structured layers anchored to specific adsorption sites on the inner surface but experiences geometric frustration due to the incompatibility between surface geometry and tetrahedral hydrogen bonding (HB). The resulting HB network is disrupted, with interfacial water forming hydrogen bonds that persist more than an order of magnitude longer than typical water−water interactions.[31] In larger-radius nanotubes ($r \geq 0.6$ nm),[32] water adopts a coaxial arrangement with mobile molecules along the center axis and strongly immobilized layers near the inner wall. The outer surface enhances the local water density up to ∼1 nm from the interface, and both inner and outer structuring are strongly influenced by nanotube curvature.

Water adsorbed on IMO at low humidity interacts with the nanotube structure, likely through HB with hydroxyl groups, leading to a red-shifted and broader O−H stretching band in infrared (IR) spectroscopy experiments.[33] Neutron scattering studies suggest that water initially adsorbs as a monolayer on the inner Si−OH surface and exhibits restricted jump diffusion between hydroxyl sites, with an estimated self-diffusion coefficient of $D \approx 1.4 \times 10^{-9}$ m^2·s^{-1}, roughly half that of bulk water.[34] As the tube fills to capacity, the geometric constraints of the narrow internal cavity immobilize the translational diffusion on the picosecond time scales accessible to neutron scattering.[34] The neutron-derived diffusion coefficient ($D \approx 1.4 \times 10^{-9}$ m^2·s^{-1}) differs from the value estimated with nuclear magnetic resonance (NMR) T_1 relaxation measurements ($D \approx 5 \times 10^{-10}$ m^2·s^{-1}), which assume ideal one-dimensional diffusion behavior inside the nanotubes.[35] To overcome the short T_2 relaxation limitations in NMR, CF_4 was used to indirectly show that diffusion along the nanotube is roughly 4 orders of magnitude greater than perpendicular to the nanotube surfaces.[36]

Challenges in directly resolving nanoconfined water populations, inconsistencies among reported diffusion coefficients, and a strong dependence on the hydration state have left an incomplete and fragmented understanding of water−IMO interactions. A key source of this ambiguity is the difficulty in disentangling the effect of geometric confinement imposed by the narrow tube diameter and specific water−

https://doi.org/10.1021/jacs.5c22784
J. Am. Chem. Soc. XXXX, XXX, XXX−XXX

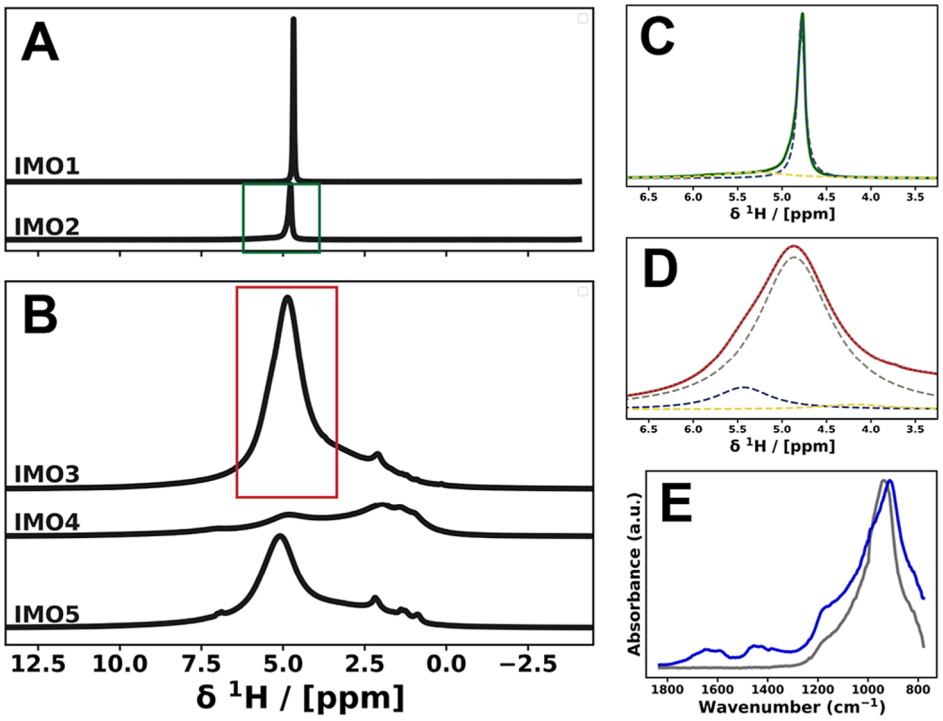

Figure 2. Water configurations of hydrated IMO via NMR and IR spectroscopy. (A) ^{1}H solution NMR spectra of samples *IMO1* (95 wt %H_2O) and *IMO2* (92 wt %H_2O) conducted at 25 °C. (B) ^{1}H solid-state NMR spectra of samples *IMO3* (40 wt %H_2O), *IMO4* (7 wt %H_2O), and *IMO5* (30 wt %H_2O), comprised of water signatures (4−6 ppm) and hydroxyl environments (0−4 ppm, 7 ppm). Solid-state NMR experiments were conducted at 60 kHz MAS with the probe temperature set to 25 °C. Spectra were normalized by sample mass with all acquisition parameters held constant. (C) NMR spectrum of sample *IMO2* (solid green line) in the region from 3.5 to 6.5 ppm (indicated by the green rectangle in A), highlighting two proton environments (colored dashed lines). (D) ^{1}H solid-state NMR spectrum of sample *IMO3* (solid red line) in the water region at 3.5 to 6.5 ppm (red rectangle in B), with deconvoluted peaks at 5.4, 4.9, and 4.1 ppm. (E) IR mapping spectrum of sample IMO3 showing a dry region (gray) and hydrated region (blue).

surface interactions governed by the chemistry of the inner wall. In this work, we directly probe the molecular-level structure and dynamics of nanoconfined water in IMOs across hydration levels ranging from fully saturated to ∼7 wt % water content (Table S1). The combined approach using solution-state and magic-angle spinning (MAS) solid-state NMR spectroscopies, NMR relaxometry, NMR diffusometry, MD simulations, and IR spectroscopy allows us to assess water mobility and local bonding environments as a function of hydration. We hypothesize that water confined within imogolite nanotubes is not a single uniform phase but partitions into distinct populations whose structure and mobility are dictated by the surface hydroxyl chemistry of the walls that bound them. To test this, we resolve these populations and quantitatively evaluate their mobilities inside and outside the nanotube, constructing a multidimensional picture of how hydration, surface binding, and tube geometry influence the behavior of nanoconfined water.

RESULTS

Water Structures in Imogolite Depend on Hydration

The structures of water in IMO nanotubes change depending on hydration levels, transitioning from bulk-like behavior at high water content to highly immobilized configurations as water is removed. Across a series of samples containing ∼95 to ∼7 wt %H_2O (Figure 1D, Table S1), we observe the emergence of distinct water environments by studying a progressive evolution of the ^{1}H NMR spectra at different hydration levels (Figure 2A,B). In the highest water content suspension (*IMO1*, with 95 wt %H_2O), the solution NMR spectrum is dominated by a single sharp resonance at 4.68 ppm, characteristic of mobile water with bulk-like dynamics. Slight dehydration to 92 wt %H_2O (*IMO2*) produces a subtle downfield shift and the appearance of a broad component at ∼5.3 ppm alongside a sharp 4.8 ppm peak (Figure 2C). The change in the solution NMR spectra between samples suggests that as the water concentration decreases, the surrounding water begins to experience configurational changes. The emergence of the broad component at 5.3 ppm indicates a distribution of more self-interacting water populations with reduced nuclear shielding, likely due to increased interfacial interactions, which lift the degeneracy of the water ^{1}H spin states.

Removal of bulk water through freeze-drying (*IMO3*, 40 wt %H_2O) or controlled dehydration (*IMO4*, 7 wt %H_2O) and rehydration (*IMO5*, 30 wt %H_2O) reveals the additional spectral signatures of immobile water and hydroxyl groups on the IMO surface. Solid-state ^{1}H NMR (60 kHz MAS) spectra for these powder samples, with no visible liquid water, show broad resonances between 4 and 6 ppm corresponding to water in restricted environments, alongside other peaks between 0 and 4 ppm assigned to Si−OH and Al−OH groups (Figures 2B,D, and S1).[37] Upon heating to produce *IMO4* and subsequent rehydration (*IMO5*), visible ^{1}H NMR peaks appear near 7 ppm. We attribute these to hydroxyl protons engaged in strong hydrogen bonding, which deshields the proton and shifts the peak downfield, consistent with prior reports of strongly perturbed hydroxyl hydrogen bonds in aluminosili-

https://doi.org/10.1021/jacs.5c22784
J. Am. Chem. Soc. XXXX, XXX, XXX−XXX

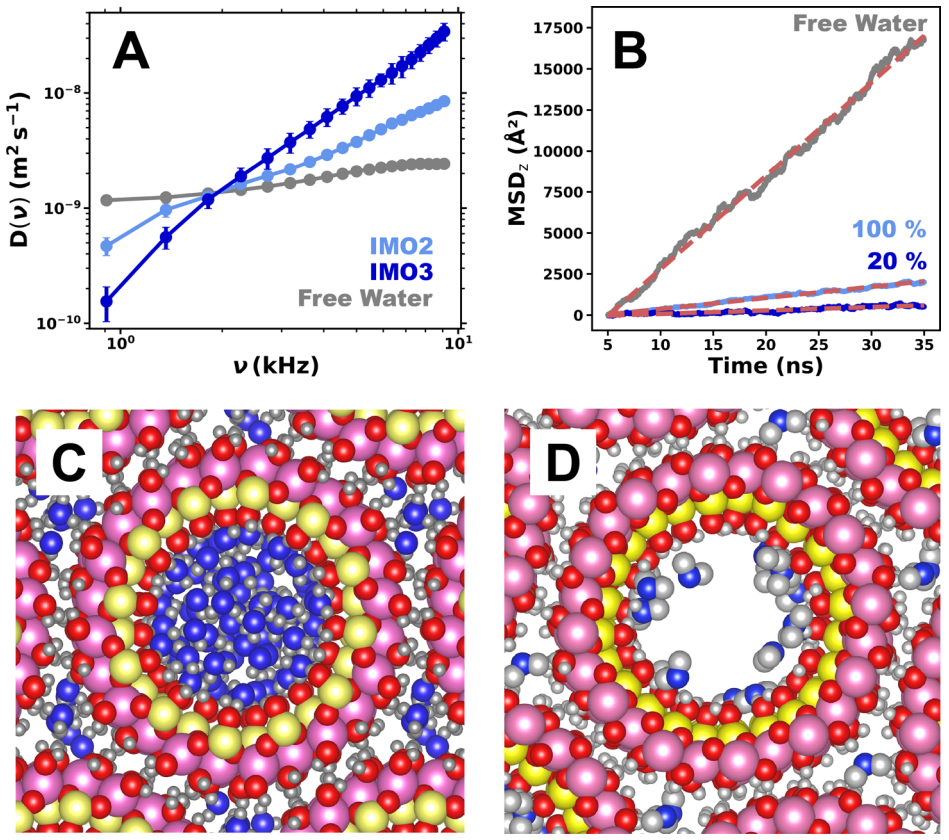

Figure 3. Diffusivity of water in IMOs. (A) MGSE D(v) spectra of free water (gray) and samples *IMO2* with 92 wt %H_2O (light blue) and *IMO3* with 40 wt %H_2O (dark blue). Error bars represent the standard error of 3 replicate measurements. MGSE experiments were conducted at room temperature. (B) MD simulations of the mean-squared displacement (MSD) of free water (gray), fully hydrated (light blue), and 20% hydrated (dark blue) IMO. The red dashed line corresponds to the linear Einstein diffusion fit. (C,D) Snapshots of MD simulations of (C) fully saturated (100% hydrated) IMO and (D) 20% hydrated IMO. Colors correspond to hydrogen (gray), water oxygen (blue), IMO oxygen (red), aluminum (pink), and silicon (yellow).

cates.[37−40] This progression from narrow, solution-like lines to broad resonances reflects the emergence of heterogeneous water populations with varying degrees of mobility and surface interactions (vide infra).

Infrared spectroscopic mapping[41] of sample *IMO3* (40 wt % H_2O) (Figure 2E) confirms the heterogeneous distribution of residual water at the submicrometer scale. Besides the dominant Si−O peaks at ∼1000 cm^{-1}, regions with detectable water (blue spectra) exhibit a distinct vibrational mode at ∼1460 cm^{-1}, along with the ∼1640 cm^{-1} O−H bending mode typical of surface-confined water, consistent with an earlier observation.[33] In contrast, adjacent regions with no measurable water signal (gray spectra) at ∼1640 cm^{-1} show no such feature. Figure S2 shows the deconvolution of the partially hydrated region, further revealing hyperfine splitting of these O−H vibrational modes. We attribute the 1460 cm^{-1} peaks to the silanol O−H scissoring modes induced by strongly bound water, consistent with our observations by ^{1}H NMR, and confirmed by first-principles simulations on hydrated imogolites.[42]

Dynamic Water Population Mobilities

The evolution of NMR and IR features with decreasing hydration reflects water reorganization among its distinct environments, revealing signatures of strongly adsorbed or restricted water. To resolve contributions from distinct adsorption sites and mobility regimes, we combine T_2 relaxometry, which captures surface-driven relaxation reflecting restricted rotational motion,[43] with modulated-gradient spin−echo (MGSE) NMR,[44] which resolves frequency-dependent diffusion dynamics. In MGSE, low-frequency gradient modulations probe slower, collective motions over longer observation times, while higher frequencies reflect increasingly local fluctuations; the asymptotic limits of the spectrum correspond to the effective diffusion coefficients associated with these dynamic regimes. Together, these MGSE and T_2 measurements disentangle the molecular origins of mobility in confined water through controlled dehydration experiments that remove the influence of mobile water populations.

Interactions with IMO surfaces restrict water mobility and produce heterogeneous water dynamics, consistent with the broader behavior of confined water.[45] In saturated samples (*IMO1* and *IMO2*), we identify three long T_2 components of ∼80, 250, and 550 ms using solution NMR relaxometry (with a lower detectable limit of 1.2 ms in this measurement), as shown in Figure S3A. This multiexponential decay reflects coexisting populations of water, from restricted to highly mobile, which we attribute to water in mesopores formed between aggregated nanotubes.[32] Partial dehydration from *IMO1* (95 wt %H_2O) to *IMO2* (92 wt %H_2O) preserves the three relaxation constants but alters the relative contribution and value of each component. The longest-lived component at 550 ± 30 ms, which we attribute to the most bulk-like water, is reduced, and the component at 270 ± 10 ms increases sharply, with a subtle shift to 240 ± 20 ms. The shortest detected T_2

https://doi.org/10.1021/jacs.5c22784
J. Am. Chem. Soc. XXXX, XXX, XXX−XXX

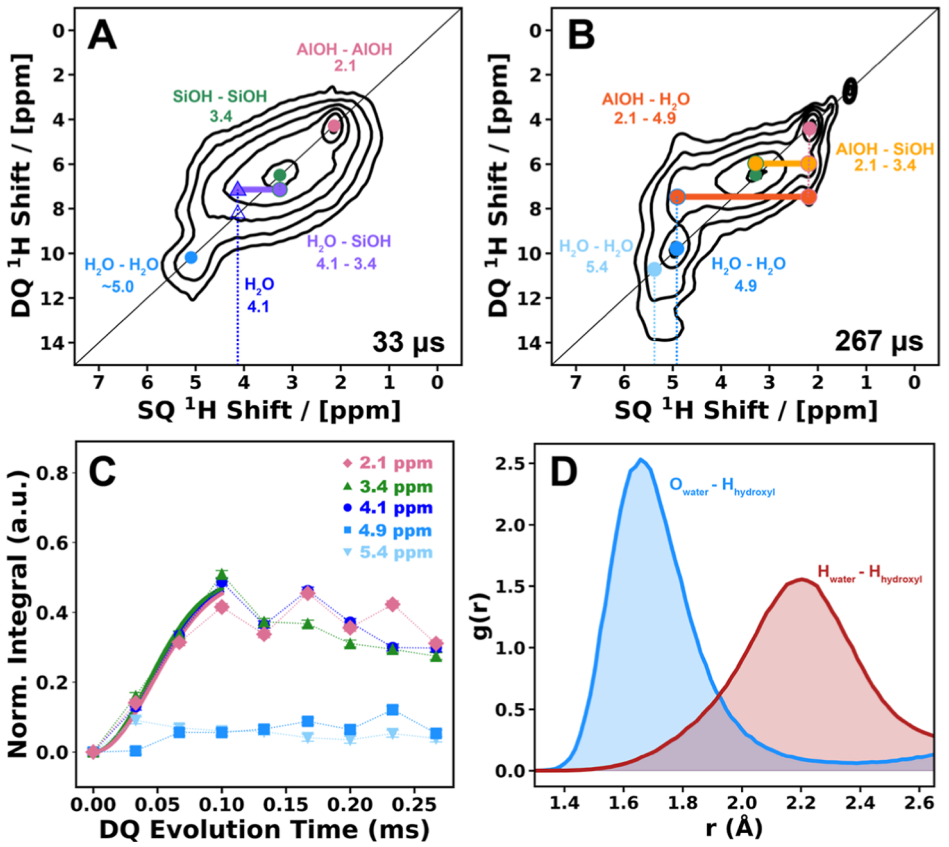

Figure 4. (A,B) ^{1}H homonuclear correlation spectroscopy of sample *IMO3* (40 wt %H_2O) conducted at 60 kHz MAS with the probe temperature set to 25 °C. (*A*) 33 μs recoupling duration. On-diagonal circles mark self-correlations of water at ∼5 ppm (blue), Si−OH at 3.4 ppm (green), and Al−OH at 2.1 ppm (pink). An off-diagonal correlation between inner surface-bound water at 4.1 ppm (triangle) and Si−OH at 3.4 ppm (circle) is shown in purple. The open triangle (dark blue) on the diagonal indicates the absent self-correlation peak for the 4.1 ppm water population. (B) 267 μs recoupling duration. On-diagonal circles mark self-correlations for Al−OH (pink), Si−OH (green), inner core water (5.4 ppm, light blue), and outer surface-bound water (4.9 ppm, blue). Off-diagonal correlations include coupling between outer-bound water (4.9 ppm) and Al−OH (orange) and between Al−OH and Si−OH (yellow). The inner-bound water (4.1 ppm) to Si−OH correlation is omitted for clarity. (C) 1D normalized homonuclear dipolar coupling build-up curve of sample *IMO3* (40 wt %H_2O) conducted at 60 kHz MAS with the probe temperature set to 25 °C. Marker colors correspond to Al−OH (2.1 ppm, pink), Si−OH (3.4 ppm, green), inner surface-bound water (4.1 ppm, dark blue), inner tube-confined water core (5.4 ppm, light blue), and outer surface-bound water (4.9 ppm, medium blue). Solid colored lines represent the second-moment approximation fit of the DQ build-up. (D) MD simulations of the radial distribution function, g(r), between inner-surface IMO hydroxyl groups and water oxygen (blue) and hydrogen (red) of the fully hydrated IMO.

also decreases from 88 ± 5 ms to 70 ± 10 ms, which is further evidence for the reorganization of water populations into more structured configurations that we observe in the 1D spectra (Figure 2A).

When bulk water is further removed (*IMO3*, 40 wt %H_2O), immobilized water populations dominate the solid-state NMR signal. Fitting of the T_2 decay yields a relaxation time of 1.01 ± 0.04 ms for the water signal (Figure S3B), orders of magnitude shorter than pure bulk water (>1 s)[46] and indicative of highly restricted mobility, likely dominated by surface binding interactions. We observe a further reduction of a dominant T_2 component in the highly dehydrated sample (*IMO4*, 7 wt % H_2O) to 0.64 ± 0.03 ms, which we attribute to a population of highly immobilized interfacial water (Figure S3C,D).

For free water, the MGSE-obtained diffusion spectrum converges to ∼2.4 × 10^{-9} $m^2{\cdot}s^{-1}$, indicated by a horizontal asymptote, and is in good agreement with the self-diffusion coefficient measured with PFG-NMR (Figure 3A).[47] By contrast, water confined in IMO (*IMO2* and *IMO3*) deviates strongly from this behavior in both the low-frequency and high-frequency regimes (Figure 3A). The lowest-frequency (or long-range) diffusion coefficient of *IMO2* (92 wt %H_2O) is 4.7 (±0.8) × 10^{-10} $m^2{\cdot}s^{-1}$, approximately 2.5× slower than free water (1.17 (±0.04) × 10^{-9} $m^2{\cdot}s^{-1}$). For *IMO3* (40 wt % H_2O), the coefficient drops further to 1.6 (±0.6) × 10^{-10} $m^2{\cdot}s^{-1}$, which is comparable to the self-diffusion coefficients of water at subzero (°C) temperatures.[48] At the highest measured frequency, which reflects short-range confinement and interfacial interactions, diffusivities of *IMO3* and *IMO2* are 3.4 (±0.6) × 10^{-8} $m^2{\cdot}s^{-1}$ and 8.49 (±0.04) × 10^{-9} $m^2{\cdot}s^{-1}$, respectively. As bulk-like water is removed, the geometric curvature and small internal radius of the nanotube likely restrict translational motion from free three-dimensional (3D) mobility to one-dimensional (1D) transport along the nanotube axis, consistent with the 3-fold reduction in low-frequency diffusivity from *IMO2* to *IMO3*. The 4-fold increase in high-frequency diffusivity, reflecting larger local fluctuations, indicates a more significant increase in molecular restriction,[49] again, likely due to the strong surface-binding interactions.

Note that our MGSE measurements, conducted for modulation frequencies of 0.5−9.1 kHz (corresponding to ∼0.1−2 ms time scales), do not reach a Fickian asymptote in

https://doi.org/10.1021/jacs.5c22784
J. Am. Chem. Soc. XXXX, XXX, XXX−XXX

either frequency limit for the IMO samples. Therefore, the reported values at the lowest measured frequency represent upper bounds on the true long-range diffusivity, while the high-frequency values represent lower bounds on the local fluctuations. Here, the accessible low-frequency limit of MGSE (corresponding to long-range motion) is constrained by T_2 relaxation. Thus, the very short T_2 of the dehydrated samples (*IMO3*−*IMO5*) limits diffusion measurements to frequencies above 0.5 kHz, preventing direct measurement of the fundamental zero-frequency diffusion limit. Nevertheless, the value at this lowest frequency is considered a close approximation.

Since MGSE reports a population-averaged diffusivity, MD simulations provide helpful context for decomposing contributions from distinct water environments. At full hydration, simulations show that water organizes into a strongly bound coaxial shell along the inner wall, clusters in the central core, and occupies interstitial regions on the outer surface (Figure 3C).[31,32] Upon dehydration, water is largely confined to these surface-bound layers (Figure 3D). Inside the nanotube, molecules near the center of the tubes exhibit higher mobility, facilitating axial anisotropic diffusion, while those adjacent to the inner walls are more restricted due to strong bonding with the surface. Applying Einstein's diffusion equation to the simulated time-dependent mean-squared displacement (MSD),[50] the calculated mean diffusion coefficients of all the water present are 3.38×10^{-10} $m^2 \cdot s^{-1}$ at full hydration and 1.04×10^{-10} $m^2 \cdot s^{-1}$ at 20% hydration (Figure 3B). MD simulations were performed using the ClayFF force field with the flexible simple point charge (SPC) water model,[51] employing the validated IMO structure and simulation protocol of an earlier study.[31] These values are in very good agreement with our experimental data, confirming that the slower diffusion arises from strong surface interactions and disrupted hydrogen bond networks as a result of 1D confinement.

Imogolite Surfaces Dictate Water Configurations

It is clear from T_2 relaxometry, MGSE diffusivity, and MD simulations that IMO surfaces influence the structures of water. The 40 wt % hydrated *IMO3* (Figure S3B) shows that the hydroxyl groups exhibit a fast transverse relaxation (T_2 = 0.96 ± 0.09 ms), and a much slower component (T_2 = 12 ± 3 ms), reflecting distinct mobility regimes at the IMO surfaces. These results provide further evidence for the heterogeneous distribution of water interacting with IMO and how dehydration shifts the balance from mobile to strongly surface-bound populations.

To further resolve these interfacially-bound water configurations and quantify $^1H-^1H$ dipolar coupling between bound water and the surface hydroxyls, we applied double-quantum (DQ) homonuclear correlation NMR[52] to *IMO3* (40 wt % H_2O).

At the shortest recoupling time (33 μs), which probes close-proximity correlations, the DQ spectrum of *IMO3* resolves diagonal (self-correlated)[52,53] peaks for water (~5 ppm), Si−OH (~3.4 ppm), and Al−OH (~2.1 ppm). A separate water resonance at 4.1 ppm appears only as an off-diagonal correlation[52,53] with the 3.4 ppm Si−OH peak (Figure 4A). The absence of a diagonal peak for this 4.1 ppm signal likely indicates a water population tightly bound to inner-surface hydroxyls, with minimal dipolar coupling with neighboring water molecules, or could potentially be the result of rapid dephasing, or specific spin geometries that lower the detection of the autocorrelated peak. At longer recoupling durations (≥267 μs), the water signal centered near ~5 ppm partially resolves into two resonances at 4.9 and 5.4 ppm (Figures 4B and S4). The 4.9 ppm peak shows cross-correlation with the 2.1 ppm Al−OH peak, consistent with water bound at the outer surface. In contrast, the 5.4 ppm peak exhibits primarily self-correlation, attributable to 1D nanoconfined water in the nanotube core. Together, these correlations establish three proton environments: inner-surface water bound to Si−OH groups (4.1 ppm), inner-core water in the nanotube cavity (5.4 ppm), and outer-surface water interacting with Al−OH sites (4.9 ppm).

We further quantify the $^1H-^1H$ dipolar couplings using point-by-point normalized DQ build-up analysis with spectral deconvolution (Figure 4C).[52] After correcting for relaxation phenomena,[52] the inner-surface water (4.1 ppm), Si−OH (3.4 ppm), and Al−OH (2.1 ppm) resonances all exhibit similar dipolar coupling constants (D_{H-H} = 32−34 kHz, Figure 4C). For the 4.1 ppm water peak, the coupling is dominated by interactions with Si−OH (Figure 4A), indicating strong bonding between water and inner-tube hydroxyl groups. Using the standard dipolar coupling constant-distance relationship

$$D_{H-H} = -\frac{\mu_0}{4\pi} \times \frac{\gamma_H^2 \hbar}{2\pi r^3} \quad (1)$$

where μ_0, γ_H, and $\hbar$ are the vacuum permeability, proton gyromagnetic ratio, and reduced Planck's constant, respectively, we derive an approximate $^1H-^1H$ distance (r) of ~1.55 ± 0.03 Å. Our DQ build-up analysis and distance approximation assume an isolated two-spin system, whereas the inner-surface water environment is inherently multispin. Therefore, the extracted $^1H-^1H$ distance (~1.55 Å) represents an effective average intermolecular separation, rather than a precise geometric measurement. However, this remarkably short effective distance is supported by MD simulations (Figure 4D) showing a minimum $H_{water} - H_{hydroxyl}$ distance of ~1.6 Å, an $O_{water} - H_{hydroxyl}$ distance of ~1.4 Å, and previous reports of water in IMOs.[42]

This effective distance is similar to the intramolecular $^1H-^1H$ distance (~1.6 Å) of a water molecule in ice I_h,[54] suggesting an unusually close separation between water and surface hydroxyl protons. Previous MD simulations predicted that the most common inner-surface adsorption geometry places water in an upright configuration above a triangular silanol adsorption site, receiving two hydrogen bonds from silanol groups and donating one to a third, while a remaining hydroxyl group dangles freely toward the nanotube core.[31] This orientation offers a plausible geometric origin for the short $^1H-^1H$ distance we observe. The very short T_2 relaxation, significantly reduced translational diffusivity, and a dipolar coupling indicating immobility on microsecond time scales point to a strongly immobilized solid-like interfacial water layer, markedly distinct from bulk liquid water.

By contrast, the inner core (5.4 ppm) and outer surface (4.9 ppm) water peaks exhibit weaker dipolar couplings and low normalized DQ plateaus of only ~0.1 compared to the expected plateau of a multispin system (I_{nDQ}~0.5) (Figure 4C). Such depressed plateau values indicate that only a fraction of these protons participate in strong dipolar correlations,[55] while the majority are more mobile and effectively decoupled. Importantly, the inner-core (5.4 ppm) resonance builds up

https://doi.org/10.1021/jacs.5c22784
J. Am. Chem. Soc. XXXX, XXX, XXX−XXX

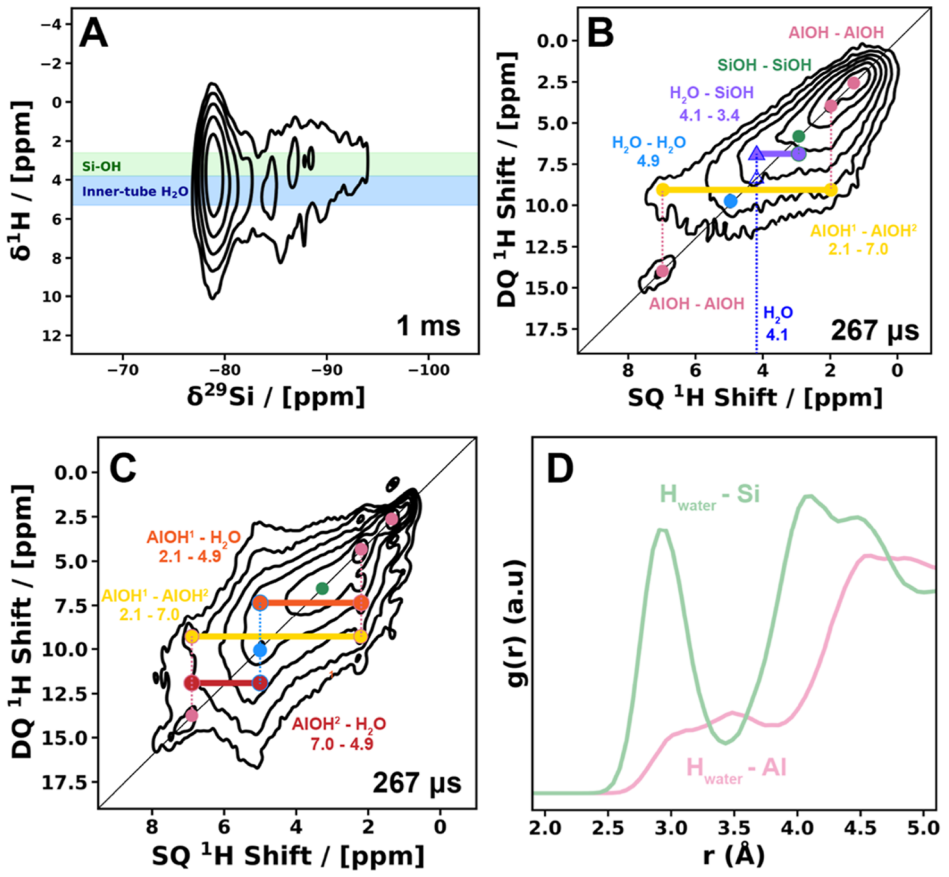

Figure 5. (A) $^{1}H-^{29}Si$ heteronuclear correlation spectroscopy of the dehydrated sample *IMO4* (7 wt %H_2O) with a contact duration of 1 ms, conducted at 60 kHz MAS with the probe temperature set to 25 °C. ^{1}H NMR regions of silanol hydroxyl (2.5−4 ppm) and inner water ^{1}H (4−5 ppm) to ^{29}Si couplings are shaded in green and blue, respectively. (B) ^{1}H homonuclear correlation spectroscopy of the dehydrated sample *IMO4* (7 wt %H_2O) with a 267 μs recoupling duration, conducted at 60 kHz MAS with the probe temperature set to 25 °C. On-diagonal circles mark self-correlations of water (blue), Si−OH (green), and Al−OH (pink). Off-diagonal correlations between inner surface-bound water at 4.1 ppm (triangle) and Si−OH (circle) are shown in purple, and an off-diagonal correlation between Al−OH sites at 7.0 and 2.1 ppm is shown in yellow. The open blue triangle on the diagonal indicates the absent self-correlation peak for the 4.1 ppm water population. (C) ^{1}H homonuclear correlation spectroscopy of the rehydrated sample *IMO5* (30 wt %H_2O) with 267 μs recoupling duration conducted at 60 kHz MAS with the probe temperature set to 25 °C. On-diagonal circles mark self-correlations of water (blue), Si−OH (green), and Al−OH (pink). Off-diagonal correlations show coupling between outer-bound water (4.9 ppm) and Al−OH sites at 2.1 ppm (orange) and 7.0 ppm (red), and correlation between the two Al−OH sites at 7.0 and 2.1 ppm (yellow). (D) The RDF from MD simulations, g(r), between water hydrogens and aluminum (pink) and silicon (green) of the fully hydrated IMO.

more rapidly than the outer-surface (4.9 ppm), indicating stronger local couplings despite its low plateau. The reduced plateau and weaker diagonal peak for the inner-core water (5.4 ppm) reflect an intermediate dynamic regime, in which water−water hydrogen bonds persist longer than in bulk, yet remain considerably more labile than those anchoring the inner-surface-bound population (4.1 ppm). The outer-surface water (4.9 ppm) exhibits the slowest buildup and the weakest dipolar coupling, indicating the most weakly bound and mobile environment within the system. This interpretation is supported by the MGSE diffusivities and is also consistent with an earlier simulation study,[56] showing that the curvature of the external imogolite surface prevents in-plane hydrogen bonds between neighboring aluminol groups, lowering the enthalpy of water adsorption and rendering the outer surface less hydrophilic than the inner silanol-rich surface despite similar underlying hydroxyl chemistry.

Deconvolution of the solid-state ^{1}H MAS NMR spectra, constrained by the 2D DQ correlation assignments, yields quantitative population fractions for the three water environments. In the hydrated state (*IMO3*, 40 wt % H_2O), the outer-surface water peak at 4.9 ppm dominates the spectrum, accounting for ∼88% of the total water ^{1}H signal, while the inner-surface (4.1 ppm) and inner-core (5.4 ppm) populations contribute ∼2.5% and 9.4%, respectively. This outer-surface dominance reflects the nanotube's geometry, which provides a larger outer surface area, and thus more hydroxyl binding sites, than the inner surface, despite their slightly weaker binding affinity. On a per-hydroxyl basis (Table S2), the outer Al−OH carries 2.1 H_2O per hydroxyl, whereas the inner Si−OH holds 0.87 H_2O per hydroxyl (including core water), corresponding to an inner-channel volumetric filling fraction of f ≈ 0.63.

Upon dehydration to *IMO4* (7 wt % H_2O), the resonances at ∼5.4 and 4.9 ppm lose approximately 81% and 89% of their intensity, respectively, while the inner-surface population at 4.1 ppm loses only ∼1%, so that its relative fraction rises from 2.5% to 18%. This is consistent with preferential removal of the more mobile outer-surface and inner-core water. The outer Al−OH occupancy falls sharply from ∼2.1 to 0.2 H_2O per hydroxyl, whereas the inner Si−OH declines more modestly,

https://doi.org/10.1021/jacs.5c22784
J. Am. Chem. Soc. XXXX, XXX, XXX−XXX

Table 1. Comparison of Water Self-Diffusion Coefficients in Imogolite Nanotubes across Methods and Hydration States

source	hydration	method	D ($m^2 \cdot s^{-1}$)	time scale	comments
			This Work		
	100%	MD	3.38×10^{-10}	5–35 ns	close-packed IMO; linear diffusion regime
	20%	MD	1.04×10^{-10}	5–35 ns	close-packed IMO; linear diffusion regime
	92 wt %	MGSE NMR	4.7×10^{-10}	2 ms (ν_{low} = 0.5 kHz)	low frequency (long-range D)
			8.5×10^{-9}	0.1 ms (ν_{high} = 9.1 kHz)	high frequency (local D)
	40 wt %	MGSE NMR	1.6×10^{-10}	2 ms (ν_{low} = 0.5 kHz)	low frequency (long-range D)
			3.4×10^{-8}	0.1 ms (ν_{high} = 9.1 kHz)	high frequency (local D)
			MD simulations (literature)		
Scalfi et al. (2018)[31]	100%	MD	3.50×10^{-10}	0.25–15 ns	close-packed IMO; N = 12 (1.6 nm)
González et al. (2020)[32]	100%	MD (axial)	$\sim(2-3) \times 10^{-10}$	1–3 ns	N = 12 (1.6 nm); multilayer approach; inner wall immobile
Zang et al. (2009)[57]	saturation	MD (axial)	$\sim 1 \times 10^{-9}$	0–8 ns (1.6 ns segments)	1.2 nm inner diameter IMO; hop diffusion mechanism
	dilute	MD (axial)	$\sim 2.3 \times 10^{-9}$	0–8 ns (1.6 ns segments)	1.2 nm inner diameter IMO; approaches bulk water at low loading
Konduri et al. (2008)[58]	~saturation	MD (axial)	$\sim 9 \times 10^{-10}$	50–600 ps	short nanotube (1.7 nm length)
Creton et al. (2008)[59]	Low	MD	~immobile	0–100 ps	inner surface molecules, shuttling motions only, no net axial diffusion
			Experimental (Literature)		
Le Caër et al. (2021)[34]	3% RH (monolayer)	QENS	1.40×10^{-9}	1–1000 ps	surface jump diffusion between Si–OH sites, axial motions
	43% RH	QENS	N/A	1–1000 ps	"rigid" hydrogen-bond network on ps time scale
Belorizky et al. (2010)[35]	~100% (internal only)	T_1 Relaxometry (FFC NMR)	5.0×10^{-10}	5 ns −8 μs	model-derived assuming ideal 1D diffusion

from ~0.87 to 0.24 H_2O per hydroxyl, with the inner-channel filling fraction dropping from f ≈ 0.63 to ≈0.17 (Table S2).

Conversely, as shown in Table S2, in the rehydrated *IMO5* (30 wt %), inner Si–OH occupancy recovers to 1.4 H_2O per hydroxyl (f ≈ 1.0), exceeding that of the outer surface (1.1 H_2O per Al–OH). This indicates that water preferentially refills the inner channel to near saturation upon rehydration with water vapor, mirroring the dehydration order in which inner-surface water is retained longest.

For *IMO3*, all three sites yield comparable T_2 values (~1 ms), likely reflecting efficient $^1H-^1H$ spin diffusion between proximate populations. However, the deconvolution of *IMO4* shows the inner-surface water (4.1 ppm) has a reduced T_2 of ~0.6 ms, while the other two sites (4.9 and 5.4 ppm) contain longer T_2 tails (~5 ms) (Figure S3C), which confirms that the inner-surface water, governed by strong interactions with the silanol interface, is indeed solid-like, and the most immobilized population within the system.

We confirm the persistence of inner-surface water by the $^1H-^{29}Si$ heteronuclear correlation (HETCOR) NMR spectrum (Figure 5A), where the residual water-proton (~4.5 ppm) intensity correlates directly with the ^{29}Si signal (−79 ppm). The DQ NMR spectrum (Figure 5B) confirms that water in *IMO4* (7 wt %H_2O) is strongly coupled to Si–OH, as evidenced by the off-diagonal correlation between Si–OH and water at 4.1 ppm. MD simulations show that upon dehydration to 7 wt %H_2O, the inner core water is removed first, leaving a persistent monolayer of water molecules strongly bound to the Si–OH surface (Figure S5). This finding is consistent with the reduced T_2 (~0.64 ms) of the water signal in *IMO4*, DQ correlation, and the observed shift of silanol vibrations, providing strong evidence that this solid-like, inner-surface water fundamentally limits the overall water mobility in imogolite systems.

The DQ spectrum (Figure 5C) of the rehydrated 30 wt % H_2O sample, *IMO5*, reveals pronounced coupling between water and Al–OH groups. The T_2 of Al–OH protons lengthens from ~1 to ~20 ms upon rehydration, consistent with enhanced local mobility due to interaction with adsorbed water (Figure S6). In contrast, the T_2 values of Si–OH and inner-surface water remain short (<5 ms) (Figure S6), suggesting that these sites are either saturated or inaccessible during the early stages of hydration. After 1 week, however, the T_2 of a Si–OH population increases to >10 ms (Figure S6), indicating that hydration of the nanotube interior likely equilibrates only over several days. This delayed equilibrium is consistent with the reported hydration isotherms of IMO.[34]

The radial distribution function (RDF) from MD simulations (Figure 5D) of fully hydrated nanotubes shows that the minimum water–Si distances are shorter than water–Al distances, indicating that the Si–OH inner surface is more hydrophilic than the Al–OH outer surface. This stronger water–Si affinity, coupled with spatial confinement within the nanotube, helps explain why inner-surface water remains tightly bound and why the outer surface experiences higher mobility (Figure 4C).

DISCUSSION AND CONCLUSION

Our results demonstrate that the properties of water in imogolite are governed by chemical interactions with IMO surface hydroxyls. The water evolves systematically with hydration state and begins to organize at high saturation into populations with varied mobility as a result of IMO surface interactions. Upon removal of bulk water, we observe a significant shift of hydroxyl vibrations and ^1H resonances, together with reductions in long-range water diffusion (1.6 (±0.6) × 10^{-10} $m^2 \cdot s^{-1}$) and T_2 relaxation (<1 ms). The surfaces of IMO partition the water into three distinct configurations, each with different properties.

https://doi.org/10.1021/jacs.5c22784
J. Am. Chem. Soc. XXXX, XXX, XXX–XXX

The inner-surface water behaves as a solid-like shell, which is immobilized by surface interactions with the Si−OH groups. This surface water is characterized by a large residual dipolar coupling constant of ∼32 kHz, a fast T_2 relaxation below 1 ms, and a remarkably short $^1H-^1H$ distance of ∼1.55 Å, reflecting severely restricted motion that persists across hydration levels. Water occupying the inner core of the nanotube forms a disrupted hydrogen-bond network due to 1D geometric confinement yet exhibits higher mobility than the inner-surface water. The outer-surface water exhibits the highest mobility and is dictated by weaker surface interactions than those on the inner surface.

Table 1 compares water self-diffusion coefficients in IMOs across different methods and hydration states, spanning nearly 9 orders of magnitude in time scale. MD simulations from our work (3.38×10^{-10} $m^2 \cdot s^{-1}$ at full hydration) are in excellent agreement with recent MD studies on nanotubes of comparable diameter.[31,32] Earlier MD studies, reporting higher diffusivities,[57,58] used shorter nanotubes of smaller diameter, older force field implementations, and probed time scales of ps to several ns. Earlier neutron scattering measurements reveal that at low hydrations (∼3% relative humidity), water undergoes surface jump diffusion between adjacent Si−OH sites, with $D = 1.4 \times 10^{-9}$ $m^2 \cdot s^{-1}$ on faster picosecond time scales,[34] likely measuring the short-range hopping processes, and they detected no diffusion at full hydration on the picosecond time scales, consistent with an earlier MD simulation study.[59] The T_1 relaxometry-derived diffusivity (5×10^{-10} $m^2 \cdot s^{-1}$, probing 5 ns − 8 μs)[35] falls between the MD and MGSE values. Notably, direct PFG-NMR measurements are lacking due to the short T_2 of immobilized water. Our MGSE diffusometry experiments uniquely access the millisecond time scale regime and disentangle local segmental motions from long-range transport through the frequency-dependent diffusion spectrum. In addition to time scale limitations, the inconsistencies in diffusion coefficients reported across methods are also the result of averaging the different water populations in hydrated IMOs, where higher-mobility inner-core and outer-surface water likely diffuse faster than the inner-surface water.

In conclusion, our results establish that water populations in IMO are governed by surface hydroxyls, which lead to heterogeneous transport in nanopores and the persistence of a solid-like Si−OH-bound interfacial water layer across a wide range of hydration states. These findings provide a mechanistic framework linking surface hydroxyl chemistry to the structural and dynamic properties of nanoconfined water, with direct consequences for how dissolved species interact with nanopore environments. More broadly, they demonstrate that surface hydroxyl chemistry can dominate water behavior in nanoporous systems, underscoring the need to account for interfacial chemistry when interpreting nanoscale water dynamics. Distinguishing confinement-driven from chemistry-driven properties remains an open challenge for further study in nanoconfined systems.

■ ASSOCIATED CONTENT

Supporting Information

The Supporting Information is available free of charge at https://pubs.acs.org/doi/10.1021/jacs.5c22784.

Experimental methods, spectral characterizations, and additional results (PDF)

■ AUTHOR INFORMATION

Corresponding Author

Zhao Hao − *Earth and Environmental Sciences Area, Lawrence Berkeley National Laboratory, Berkeley, California 94720, United States*; Email: zhao@lbl.gov

Authors

Xander B. Fleming − *Earth and Environmental Sciences Area, Lawrence Berkeley National Laboratory, Berkeley, California 94720, United States*; orcid.org/0009-0006-0102-5375

Sophia N. Fricke − *Department of Chemical and Biomolecular Engineering, University of California, Berkeley, California 94720, United States*; orcid.org/0000-0002-0183-466X

Navya Singh − *Earth and Environmental Sciences Area, Lawrence Berkeley National Laboratory, Berkeley, California 94720, United States*

Raynald Giovine − *Pines Magnetic Resonance Center - Core Facility, College of Chemistry, University of California, Berkeley, California 94720, United States*; orcid.org/0000-0002-7208-6929

Pierre Picot − *Université Paris-Saclay, CEA, CNRS, NIMBE/LIONS, 91191 Gif-sur-Yvette, France*; orcid.org/0000-0001-8716-9463

Hasan Celik − *Pines Magnetic Resonance Center - Core Facility, College of Chemistry, University of California, Berkeley, California 94720, United States*

Jeffrey A. Reimer − *Department of Chemical and Biomolecular Engineering, University of California, Berkeley, California 94720, United States*

Benjamin Gilbert − *Earth and Environmental Sciences Area, Lawrence Berkeley National Laboratory, Berkeley, California 94720, United States*; orcid.org/0000-0003-0853-0826

Complete contact information is available at: https://pubs.acs.org/10.1021/jacs.5c22784

Notes

The authors declare no competing financial interest.

■ ACKNOWLEDGMENTS

This work is supported by the U.S. Department of Energy, Office of Science, Office of Basic Energy Sciences, Chemical Sciences, Geosciences, and Biosciences Division, under Award Number DE-AC02-05CH11231. We thank Dr. Frédéric Gobeaux for the cryo-TEM image that was made thanks to "Investissements d'Avenir" LabEx PALM (ANR-10-LABX0039-PALM). We thank Dr. Piotr Zarzycki for helpful discussions regarding molecular dynamics modeling. IR data were collected at infrared beamlines of the Advanced Light Source (ALS), a U.S. DOE Office of Science User Facility under contract no. DE-AC02-05CH11231. We thank Pines Magnetic Resonance Center's Core NMR Facility (PMRC Core) for spectroscopic assistance. The instrument used in this work was supported by the National Science Foundation under Grant No. 2018784. S.N.F. gratefully acknowledges support as a Pines Magnetic Resonance Center postdoctoral fellow.

■ REFERENCES

(1) Corti, H. R.; Appignanesi, G. A.; Barbosa, M. C.; Bordin, J. R.; Calero, C.; Camisasca, G.; Elola, M. D.; Franzese, G.; Gallo, P.; Hassanali, A.; Huang, K.; Laria, D.; Menéndez, C. A.; de Oca, J. M. M.; Longinotti, M. P.; Rodriguez, J.; Rovere, M.; Scherlis, D.; Szleifer,

I. Structure and Dynamics of Nanoconfined Water and Aqueous Solutions. *Eur. Phys. J. E* **2021**, *44* (11), 136.
(2) Tsimpanogiannis, I. N.; Moultos, O. A.; Franco, L. F. M.; Spera, M. B. de M.; Erdős, M.; Economou, I. G. Self-Diffusion Coefficient of Bulk and Confined Water: A Critical Review of Classical Molecular Simulation Studies. *Mol. Simul.* **2019**, *45* (4−5), 425−453.
(3) Chakraborty, S.; Kumar, H.; Dasgupta, C.; Maiti, P. K. Confined Water: Structure, Dynamics, and Thermodynamics. *Acc. Chem. Res.* **2017**, *50* (9), 2139−2146.
(4) Algara-Siller, G.; Lehtinen, O.; Wang, F. C.; Nair, R. R.; Kaiser, U.; Wu, H. A.; Geim, A. K.; Grigorieva, I. V. Square Ice in Graphene Nanocapillaries. *Nature* **2015**, *519* (7544), 443−445.
(5) Kapil, V.; Schran, C.; Zen, A.; Chen, J.; Pickard, C. J.; Michaelides, A. The First-Principles Phase Diagram of Monolayer Nanoconfined Water. *Nature* **2022**, *609* (7927), 512−516.
(6) Xia, Q.; Pan, Y.; Liu, B.; Zhang, X.; Li, E.; Shen, T.; Li, S.; Xu, N.; Ding, J.; Wang, C.; Vecitis, C. D.; Gao, G. Solar-Driven Abnormal Evaporation of Nanoconfined Water. *Sci. Adv.* **2024**, *10* (22), No. eadj3760.
(7) Knight, A. W.; Kalugin, N. G.; Coker, E.; Ilgen, A. G. Water Properties under Nano-Scale Confinement. *Sci. Rep.* **2019**, *9* (1), 8246.
(8) Gallo, P.; Rovere, M.; Chen, S.-H. Anomalous Dynamics of Water Confined in MCM-41 at Different Hydrations. *J. Phys.: Condens. Matter* **2010**, *22* (28), 284102.
(9) Calero, C.; Franzese, G. Water under Extreme Confinement in Graphene: Oscillatory Dynamics, Structure, and Hydration Pressure Explained as a Function of the Confinement Width. *J. Mol. Liq.* **2020**, *317*, 114027.
(10) Pan, J.; Xiao, S.; Zhang, Z.; Wei, N.; He, J.; Zhao, J. Nanoconfined Water Dynamics in Multilayer Graphene Nanopores. *J. Phys. Chem. C* **2020**, *124* (32), 17819−17828.
(11) Malfait, B.; Jani, A.; Mietner, J. B.; Lefort, R.; Huber, P.; Fröba, M.; Morineau, D. Influence of Pore Surface Chemistry on the Rotational Dynamics of Nanoconfined Water. *J. Phys. Chem. C* **2021**, *125* (30), 16864−16874.
(12) Fumagalli, L.; Esfandiar, A.; Fabregas, R.; Hu, S.; Ares, P.; Janardanan, A.; Yang, Q.; Radha, B.; Taniguchi, T.; Watanabe, K.; Gomila, G.; Novoselov, K. S.; Geim, A. K. Anomalously Low Dielectric Constant of Confined Water. *Science* **2018**, *360* (6395), 1339−1342.
(13) Coelho, F. M.; Mercier Franco, L. F. The Interplay between Dynamics and Structure on the Dielectric Tensor of Nanoconfined Water: Surface Charge and Salinity Effect. *J. Phys. Chem. B* **2024**, *128* (47), 11759−11767.
(14) Dufils, T.; Schran, C.; Chen, J.; K. Geim, A.; Fumagalli, L.; Michaelides, A. Origin of Dielectric Polarization Suppression in Confined Water from First Principles. *Chem. Sci.* 2024, *15*(2), 516−527.
(15) Mondal, S.; Bagchi, B. Dielectric Properties of Nanoconfined Water. *J. Chem. Phys.* **2024**, *161* (22), 220901.
(16) Ilgen, A. G.; Kabengi, N.; Smith, J. G.; Sanchez, K. M. M. Ion Solvation as a Predictor of Lanthanide Adsorption Structures and Energetics in Alumina Nanopores. *Commun. Chem.* **2023**, *6* (1), 172.
(17) Chogani, A.; King, H. E.; Tutolo, B.; Živković, A.; Plümper, O. Geochemistry of Lithospheric Aqueous Fluids Modified by Nano-confinement. *Nat. Geosci.* **2025**, *18* (2), 191−196.
(18) Phan, A.; Cole, D. R.; Weiß, R. G.; Dzubiella, J.; Striolo, A. Confined Water Determines Transport Properties of Guest Molecules in Narrow Pores. *ACS Nano* **2016**, *10* (8), 7646−7656.
(19) Muñoz-Santiburcio, D.; Marx, D. On the Complex Structural Diffusion of Proton Holes in Nanoconfined Alkaline Solutions within Slit Pores. *Nat. Commun.* **2016**, *7* (1), 12625.
(20) Stolte, N.; Hou, R.; Pan, D. Nanoconfinement Facilitates Reactions of Carbon Dioxide in Supercritical Water. *Nat. Commun.* **2022**, *13* (1), 5932.
(21) Abdolhosseini Qomi, M. J.; Miller, Q. R. S.; Zare, S.; Schaef, H. T.; Kaszuba, J. P.; Rosso, K. M. Molecular-Scale Mechanisms of CO2 mineralization in Nanoscale Interfacial Water Films. *Nat. Rev. Chem.* **2022**, *6* (9), 598−613.
(22) Becker, M. R.; Netz, R. R. Interfacial vs Confinement Effects in the Anisotropic Frequency-Dependent Dielectric, THz and IR Response of Nanoconfined Water. *J. Chem. Phys.* **2024**, *161* (22), 224704.
(23) Dasgupta, S.; Saha, S.; Paesani, F. Reactivity of Nanoconfined Water Is Modulated by the Properties of Confining Materials. *J. Phys. Chem. Lett.* **2025**, *16* (46), 11996−12004.
(24) Wang, Y.; Tang, F.; Yu, X.; Chiang, K.-Y.; Yu, C.-C.; Ohto, T.; Chen, Y.; Nagata, Y.; Bonn, M. Interfaces Govern the Structure of Angstrom-Scale Confined Water Solutions. *Nat. Commun.* **2025**, *16* (1), 7288.
(25) Sit, I.; Fashina, B. T.; Baldo, A. P.; Leung, K.; Grassian, V. H.; Ilgen, A. G. Formic and Acetic Acid pKa Values Increase under Nanoconfinement. *RSC Adv.* **2023**, *13* (33), 23147−23157.
(26) Yoshinaga, N.; Aomine, S. Imogolite in Some Ando Soils. *Soil Sci. Plant Nutr.* **1962**, *8* (3), 22−29.
(27) Wada, K.; Yoshinaga, N. The Structure of Imogolite. *Am. Mineral.* **1969**, *54* (1−2), 50−71.
(28) Picot, P.; Gobeaux, F.; Charpentier, T.; Belloni, L.; Takahara, A.; Wada, S.-I.; Thill, A. Diameter and Chirality of Natural and Synthetic Imogolite. *Appl. Clay Sci.* **2024**, *258*, 107497.
(29) D'Angelo, A.; Paineau, E.; Rouzière, S.; Elkaim, E.; Goldmann, C.; Toquer, D.; Rols, S.; Launois, P. The Atomic Structure of Imogolite Nanotubes: A 50 Years Old Issue Reinvestigated by X-Ray Scattering Experiments and Molecular Dynamics Simulations. *Appl. Clay Sci.* **2023**, *242*, 107043.
(30) Dhaini, A.; Geneste, A.; Raad, F. A.; Picot, P.; Martin-Gassin, G.; Prelot, B.; Gassin, P.-M.; Trens, P.; Thill, A.; Zajac, J. Dried Hybrid Imogolite Nanotubes as Solids with a Changeable Surface Area: An Insight into Textural Properties Based on the Correlation between Nitrogen Gas Adsorption, Immersion Calorimetry into Water, and Small Angle X-Ray Scattering. *Phys. Chem. Chem. Phys.* **2024**, *26* (36), 23835−23845.
(31) Scalfi, L.; Fraux, G.; Boutin, A.; Coudert, F.-X. Structure and Dynamics of Water Confined in Imogolite Nanotubes. *Langmuir* **2018**, *34* (23), 6748−6756.
(32) González, R. I.; Rojas-Nunez, J.; Valencia, F. J.; Munoz, F.; Baltazar, S. E.; Allende, S.; Rogan, J.; Valdivia, J. A.; Kiwi, M.; Ramírez, R.; Greathouse, J. A. Imogolite in Water: Simulating the Effects of Nanotube Curvature on Structure and Dynamics. *Appl. Clay Sci.* **2020**, *191*, 105582.
(33) Liao, Y.; Picot, P.; Lainé, M.; Brubach, J.-B.; Roy, P.; Thill, A.; Le Caër, S. Tuning the Properties of Confined Water in Standard and Hybrid Nanotubes: An Infrared Spectroscopic Study. *Nano Res.* **2018**, *11* (9), 4759−4773.
(34) Le Caër, S.; Pignié, M.-C.; Berrod, Q.; Grzimek, V.; Russina, M.; Carteret, C.; Thill, A.; Zanotti, J.-M.; Teixeira, J. Dynamics in Hydrated Inorganic Nanotubes Studied by Neutron Scattering: Towards Nanoreactors in Water. *Nanoscale Adv.* **2021**, *3* (3), 789−799.
(35) Belorizky, E.; Fries, P. H.; Guillermo, A.; Poncelet, O. Almost Ideal 1D Water Diffusion in Imogolite Nanotubes Evidenced by NMR Relaxometry. *ChemPhysChem* **2010**, *11* (9), 2021−2026.
(36) Dvoyashkin, M.; Zang, J.; Yucelen, G. I.; Katihar, A.; Nair, S.; Sholl, D. S.; Bowers, C. R.; Vasenkov, S. Diffusion of Tetrafluoromethane in Single-Walled Aluminosilicate Nanotubes: Pulsed Field Gradient NMR and Molecular Dynamics Simulations. *J. Phys. Chem. C* **2012**, *116* (40), 21350−21355.
(37) Yucelen, G. I.; Choudhury, R. P.; Leisen, J.; Nair, S.; Beckham, H. W. Defect Structures in Aluminosilicate Single-Walled Nanotubes: A Solid-State Nuclear Magnetic Resonance Investigation. *J. Phys. Chem. C* **2012**, *116* (32), 17149−17157.
(38) Hunger, M. Multinuclear Solid-State NMR Studies of Acidic and Non-Acidic Hydroxyl Protons in Zeolites. *Solid State Nucl. Magn. Reson.* **1996**, *6* (1), 1−29.
(39) Brunner, E.; Beck, K.; Koch, M.; Heeribout, L.; Karge, H. G. Verification and Quantitative Determination of a New Type of

Brønsted Acid Sites in H-ZSM-5 by 1H Magic-Angle Spinning Nuclear Magnetic Resonance Spectroscopy. *Microporous Mater.* **1995**, *3* (4), 395−399.
(40) Beck, L. W.; White, J. L.; Haw, J. F. 1H{27Al} Double-Resonance Experiments in Solids: An Unexpected Observation in the 1H MAS Spectrum of Zeolite HZSM-5. *J. Am. Chem. Soc.* **1994**, *116* (21), 9657−9661.
(41) Marchetti, A.; Beltran, V.; Nuyts, G.; Borondics, F.; De Meyer, S.; Van Bos, M.; Jaroszewicz, J.; Otten, E.; Debulpaep, M.; De Wael, K. Novel Optical Photothermal Infrared (O-PTIR) Spectroscopy for the Noninvasive Characterization of Heritage Glass-Metal Objects. *Sci. Adv.* **2022**, *8* (9), No. eabl6769.
(42) Monet, G.; Paineau, E.; Chai, Z.; S. Amara, M.; Orecchini, A.; Jimenéz-Ruiz, M.; Ruiz-Caridad, A.; Fine, L.; Rouzière, S.; Liu, L.-M.; Teobaldi, G.; Rols, S.; Launois, P. Solid Wetting-Layers in Inorganic Nano-Reactors: The Water in Imogolite Nanotube Case. *Nanoscale Adv.* 2020, *2*(5), 1869−1877.
(43) Levitt, M. H. *Spin Dynamics: Basics of Nuclear Magnetic Resonance*; John Wiley & Sons, 2013.
(44) Callaghan, P. T.; Stepišnik, J. Frequency-Domain Analysis of Spin Motion Using Modulated-Gradient NMR. *J. Magn. Reson. A* **1995**, *117* (1), 118−122.
(45) Xia, Y.; Cho, H.; Deo, M.; Risbud, S. H.; Bartl, M. H.; Sen, S. Layer-by-Layer Freezing of Nanoconfined Water. *Sci. Rep.* **2020**, *10* (1), 5327.
(46) Carr, H. Y.; Purcell, E. M. Effects of Diffusion on Free Precession in Nuclear Magnetic Resonance Experiments. *Phys. Rev.* **1954**, *94* (3), 630−638.
(47) Holz, M.; Heil, S. R.; Sacco, A. Temperature-Dependent Self-Diffusion Coefficients of Water and Six Selected Molecular Liquids for Calibration in Accurate 1H NMR PFG Measurements. *Phys. Chem. Chem. Phys.* **2000**, *2* (20), 4740−4742.
(48) Gillen, K. T.; Douglass, D. C.; Hoch, M. J. R. Self-Diffusion in Liquid Water to − 31°C. *J. Chem. Phys.* **1972**, *57* (12), 5117−5119.
(49) Fricke, S. N.; Salgado, M.; Haber, S.; Demarteau, J.; Hua, M.; Song, A.-Y.; Helms, B. A.; Reimer, J. A. Diffusion Power Spectra as a Window into Dynamic Materials Architecture. *Sci. Adv.* **2025**, *11* (15), No. eadt6144.
(50) Einstein, A. Über Die von Der Molekularkinetischen Theorie Der Wärme Geforderte Bewegung von in Ruhenden Flüssigkeiten Suspendierten Teilchen. *Ann. Phys.* **1905**, *322* (8), 549−560.
(51) Berendsen, H. J. C.; Grigera, J. R.; Straatsma, T. P. The Missing Term in Effective Pair Potentials. *J. Phys. Chem.* **1987**, *91* (24), 6269−6271.
(52) Saalwächter, K.; Lange, F.; Matyjaszewski, K.; Huang, C.-F.; Graf, R. BaBa-Xy16: Robust and Broadband Homonuclear DQ Recoupling for Applications in Rigid and Soft Solids up to the Highest MAS Frequencies. *J. Magn. Reson.* **2011**, *212* (1), 204−215.
(53) Zhang, R.; Pandey, M. K.; Nishiyama, Y.; Ramamoorthy, A. A Novel High-Resolution and Sensitivity-Enhanced Three-Dimensional Solid-State NMR Experiment Under Ultrafast Magic Angle Spinning Conditions. *Sci. Rep.* **2015**, *5* (1), 11810.
(54) Kuhs, W. F.; Lehmann, M. S. The Structure of Ice-Ih. In *Water Science Reviews 2: Crystalline Hydrates*; Water Science Review; Franks, F., Ed.; Cambridge University Press: Cambridge, 1986; Vol. 2, pp 1−66.
(55) Saalwächter, K.; Ziegler, P.; Spyckerelle, O.; Haidar, B.; Vidal, A.; Sommer, J.-U. ^{1}H Multiple-Quantum Nuclear Magnetic Resonance Investigations of Molecular Order Distributions in Poly(Dimethylsiloxane) Networks: Evidence for a Linear Mixing Law in Bimodal Systems. *J. Chem. Phys.* **2003**, *119* (6), 3468−3482.
(56) Fernandez-Martinez, A.; Tao, J.; Wallace, A. F.; Bourg, I. C.; Johnson, M. R.; De Yoreo, J. J.; Sposito, G.; Cuello, G. J.; Charlet, L. Curvature-Induced Hydrophobicity at Imogolite−Water Interfaces. *Environ. Sci. Nano* **2020**, *7* (9), 2759−2772.
(57) Zang, J.; Konduri, S.; Nair, S.; Sholl, D. S. Self-Diffusion of Water and Simple Alcohols in Single-Walled Aluminosilicate Nanotubes. *ACS Nano* **2009**, *3* (6), 1548−1556.
(58) Konduri, S.; Tong, H. M.; Chempath, S.; Nair, S. Water in Single-Walled Aluminosilicate Nanotubes: Diffusion and Adsorption Properties. *J. Phys. Chem. C* **2008**, *112* (39), 15367−15374.
(59) Creton, B.; Bougeard, D.; Smirnov, K. S.; Guilment, J.; Poncelet, O. Molecular Dynamics Study of Hydrated Imogolite. *Phys. Chem. Chem. Phys.* **2008**, *10* (32), 4879−4888.

https://doi.org/10.1021/jacs.5c22784
J. Am. Chem. Soc. XXXX, XXX, XXX−XXX